Estimating CO_2 Emissions from Large Cities using Low-Cost Sensors and Small Drone Technology

Siona Prasad

Abstract

Anthropogenic emissions of carbon dioxide (CO_2) have resulted in the build-up of greenhouse gas concentrations responsible for climate change. An accurate and efficient measurement strategy to estimate greenhouse gas emissions from megacities does not currently exist. Existing greenhouse gas sensor technology is too heavy and expensive for large-scale use in urban areas, current platforms for measurement are limited, and atmospheric modeling techniques are computationally inefficient.

In this report, I discuss the construction and calibration of an inexpensive CO_2 sensor for atmospheric measurement and multispectral camera for monitoring vegetation. A small low-powered drone was designed and built to serve as a stable platform for accurate measurements. Finally, I propose an atmospheric dispersion model and efficient inversion techniques to estimate emission inventories for large cities using sensor measurements. Low-cost sensor data compared favorably with state-of-the-art instruments (correlation factor $=.99$), and exhibited expected diurnal cycles and traffic patterns. The mathematical model successfully combined sensor data with meteorological data and predicted a CO_2 emission inventory for Washington DC. The inventory showed a large contribution from the transportation sector. Uncertainty reduction in the regions close to measurement locations were as high as 90 %.

I demonstrate a top-down methodology to measure city-wide CO_2 emissions by combining low-cost lightweight sensors, small drone technology and plume dispersion modeling, taking the first step to enforcing mitigation strategies and combating climate change.

1   Introduction

Scientific evidence for warming of the climate system is unequivocal [1, 2]. Comprehensive assessments of our current and potential future climates clearly indicate that global warming attributable to greenhouse gas emissions from human activities is a serious problem [3]. With economic, environmental, agricultural and political dimensions, the anthropogenic warming of our planet threatens nearly every aspect of our daily lives [4].

The greenhouse effect is a natural event that heats the Earth's surface and atmosphere [5]. As UV radiation energy from the sun passes through the atmosphere, 19% is absorbed by clouds, 26% is reflected back into space, and the remaining solar energy is used to heat the Earth's surface. The Earth's surface in-turn radiates this energy back towards space in the form of infrared radiation. However, the majority of this reflected energy is absorbed by greenhouse gases (GHGs) such as Carbon Dioxide (CO_2) and Methane (CH_4) in the Earth's atmosphere. This causes large amounts of heat energy to be added to the atmosphere and to be directed back to its surface, where it once again heats the ground. This cycle continues, resulting in an accumulation of heat in the atmosphere that can affect the balance of ecosystems worldwide and is believed to be the cause of global warming [6, 7].

Due to its abundance and longevity, CO_2 is considered the most important greenhouse gas. Human activities such as burning fossil fuels, deforestation and transportation release large amounts of CO_2 (around 30 billion tons per year) and have resulted in the steadily increasing CO_2 concentrations [5] in our atmosphere as seen in the Keeling Curve (Figure 1a). While steady increases of CO_2 in the atmosphere contribute to global warming, sources of CO_2 are not uniformly distributed across terrestrial and aquatic ecosystems; often, the highest fluxes come from localized hotspots. Most often these hotspots are highly populated large cities (Figure 1b) with high energy demands and extensive industrial and sociological activity [8]. A United Nations report reveals that while the world's cities cover 2% of global land area, they account for a staggering 70% of greenhouse gas emissions. Statistics indicate that the 40 largest cities in the world account for more GHG emissions than China and the United States together. The ability to measure and quantify CO_2 emissions from large cities is a crucial first step in enforcing mitigation strategies and lowering the risk of global

warming.

There are two basic approaches [9] to measuring the flux of greenhouse gases. The "bottom-up" approach takes local data at a municipal level, even gathering information from specific sources (power plants or landfills), and proper emission factors to assess hourly emissions [10]. "Bottom-up" approaches are time consuming, expensive and difficult to perform on a continuous basis. On the other hand, "top-down" approaches are based on atmospheric measurement of GHG concentrations combined with atmospheric transport and dispersion models in an inversion framework to attribute emissions. Top-down inversions are an accurate and independent approach for estimating emission inventories [9].
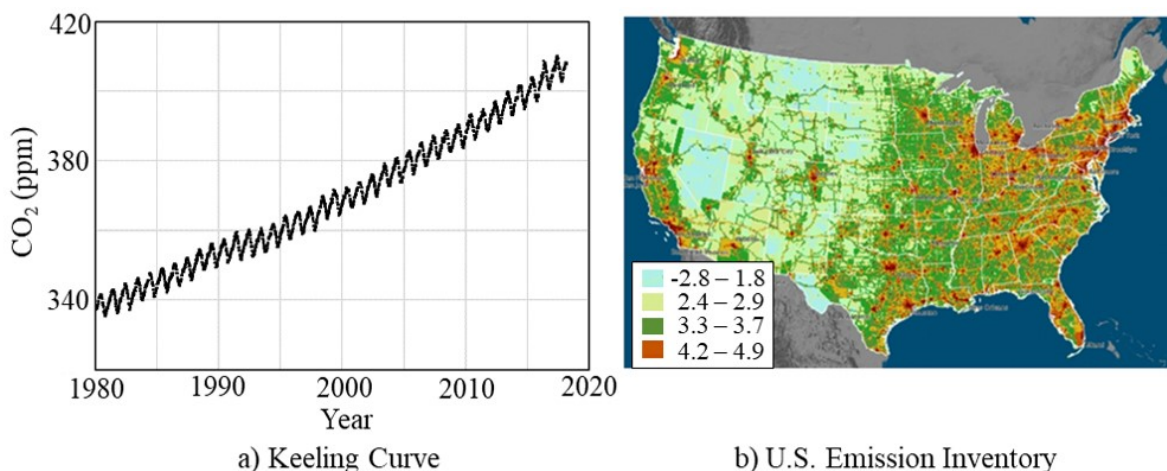

a) Keeling Curve

b) U.S. Emission Inventory

Figure 1: a) Monthly averaged CO_2 data measured at the Manua Loa Observatory, Hawaii [11] since 1980. Data obtained from `www.esrl.noaa.gov/gmd/ccgg/trends/`. b) U.S. fossil fuel CO_2 emissions [10] for the year 2002 represented on a $10\,km \times 10\,km$ grid (units: log_{10} ktC/100 km^2/year), indicating large emissions from metropolitan areas [8].

Problem, Hypothesis and Impact

In a city, greenhouse gas sources range from power plants and transportation to landfills and residential areas. In order to accurately characterize the emissions from all these sources through a top-down approach, thousands of atmospheric measurements are required. Sensors must be low-cost, in order to make high-volume deployment feasible, yet still maintain accuracy. Currently, no existing sensor fits both of these goals [12]-[15]. I hypothesize that a network of low-cost sensors that can make accurate greenhouse gas measurements in the entire atmospheric boundary layer are needed to estimate city wide emissions and in-

form mitigation efforts. In this research report, I detail the development of low-cost sensors mounted on drones to make accurate CO_2 measurements.

In order to estimate emissions from sensor measurements [5], atmospheric dispersion models and inversion tools are necessary. Current approaches based on numerical weather prediction [16] are computationally expensive and memory intensive. Here, I describe the development of simple, efficient chemical transport models to perform inversions and compute uncertainty estimates.

Sources in a city are not always all anthropogenic - biologically mediated sources/sinks such as forests and vegetation are interspersed throughout urban areas [3, 4]. Even more, the biological ecosystem is highly dynamic, varying on both a temporal and spatial scale. For example, photosynthetic activity varies based on the type of vegetation, time of year, and local weather conditions. Estimating the biological contribution to the carbon cycle is essential to properly assessing emissions in big cities. In this paper, I present an in-expensive remote sensing camera for differentiating between anthropogenic and biogenic emissions.

The goal of this report is to develop and demonstrate a top-down methodology for quantifying CO_2 emissions from large cities such as Washington DC. I propose the use of low-cost sensors and multispectral cameras mounted on small drones to make accurate measurements, as well as an efficient algorithm for atmospheric dispersion to estimate CO_2 emissions and the corresponding uncertainties. The ability to measure and attribute emissions to specific sources in a city is a crucial first step in determining the effectiveness of mitigation strategies and combating the effects of climate change. Through the development and deployment of low-cost sensors, measurement platforms, efficient mathematical models and inversion techniques, I have initiated an effort to reduce emissions from large cities.

2 Methodology

In this section, I will detail the development and calibration of a low-cost CO_2 sensor and multispectral camera. The process of building, programming and testing a low-powered drone to serve as a platform for the sensors is discussed. I review the costs, weights and specification of the sensors, drone parts and batteries to emphasize their suitability for con-

tinuous, accurate, outdoor measurements of CO_2. Finally, I present a mathematical model for atmospheric transport and an inversion framework to estimate emissions and quantify uncertainty.

2.1 Construction and Calibration of Carbon-Dioxide Sensor

The development of a CO_2 sensor will be illustrated in three steps: construction, calibration and testing. The sensor is based on non-dispersive infrared technology (NDIR). The main components of an NDIR sensor (shown schematically in Figure 2a) include an infrared light source, a sample chamber, a light filter and detector. Atmospheric gases fill the sample chamber through small pores in its membrane and infrared light is shot through the chamber toward the detector by the IR light source. According to the Beer-Lambert's law, the gas in the chamber causes absorption of specific wavelengths of the IR light, and the attenuation of these wavelengths can be detected at the end of the chamber. The optical filter just in front of the detector eliminates all light wavelengths except those that CO_2 can absorb.
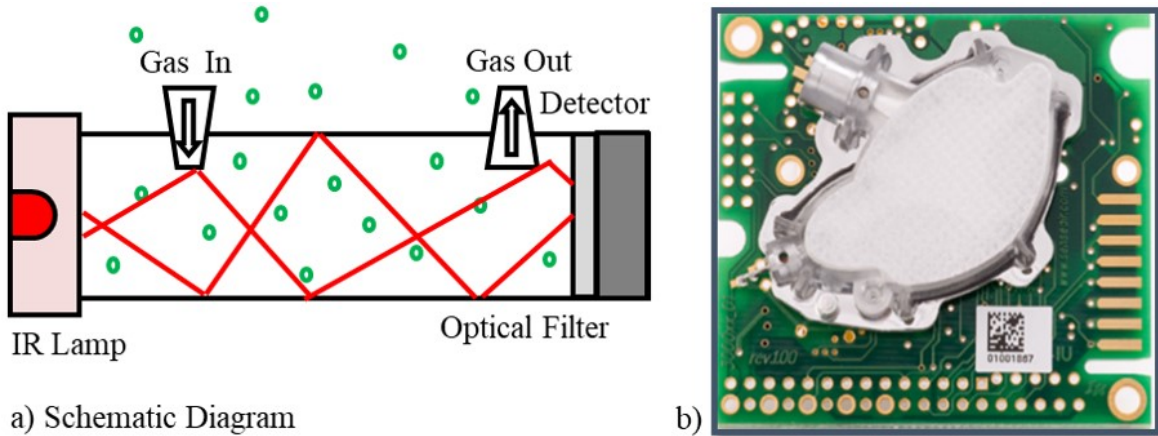

Figure 2: a) Schematic diagram of non-dispersive infrared technology. b) Image of the CO_2 sensor. Arduino board and data transmission units are not shown.

The NDIR sensor (Figure 2b) was built using an Arduino Uno board as the data collection and interpretation platform. The sensor was connected to a Raspberry Pi unit consisting of a CO_2 sensor module to detect the gas levels, a CC3000 breakout board and transmission unit. Power supply was provided by the VIN pin connected to the Arduino 5V slot.

The sensor was calibrated in three ways: 1) the nitrogen method, 2) the fresh air method

and 3) Zero calibration method. Calibration using nitrogen involves exposing the sensor to a known gas, typically 100 percent nitrogen. Although this method was accurate, it was also very expensive to achieve a pure nitrogen environment for the sensor. In the fresh-air method, the sensor was set to 200 ppm. Typical atmospheric levels of CO_2 are 390 ppm. After the sensor acclimated to outdoor values, 200 ppm was subtracted from the newly calculated offset value. Finally, the zero-calibration method was based on feeding the sensor a known free gas sample through a tube in one of two openings of the sensor. The gas was circulated for two minutes and when stabilized, the zero-calibration function was triggered.

Table 1: Comparison of performance characteristics for commercially available sensors [12]-[15] with the currently used low-cost sensor

Specification	LGR[15]	Picarro[12] G2401	MQ4[14] Arduino	Li7700[13]	**NDIR Sensor**
Accuracy (ppb)	± 2	± 1	±30,000	± 5	± 15
Range (ppm)	0–1000	0–1000	1000–5000	0–3000	0–10000
Temperature ^{0}C	5–45	-10–45	20–25	-25–50	0–50
Pressure (kPa)	0.01–100	40–133	<100	50–110	<100
Humidity(%)	<98	<99	0–95	0–99	0–95
Measurement Technology	Cavity Enhanced Absorption	Cavity Ring Down	Electro-chemical	Cavity Ring Down	Non-dispersive Infrared
Cost	$ 60,000	$ 60,000	$ 12	$ 60,000	$ 200
Weight	25 kg	25 kg	50 g	25 kg	64 g

The NDIR sensor was tested indoors & outdoors in stationary mode, as well as on mobile platforms (discussed later). The sensor and accessories cost $ 200, and have a total weight of 64 g. The accuracy of the CO_2 sensor was found to be ± 15 ppb. Table 1 shows a comparison of the performance characteristics of the NDIR sensor with commercially available sensors. The LiCOR [13] and Picarro [12] sensors are based on Cavity Ring Down Spectroscopy, and exhibit very high accuracy ($\pm 2\,ppb$). However, these sensors cost over $ 60,000 and weigh approximately 25 kg, which makes them less suitable for deployment in a dense network. The LGR [15] sensor based on Cavity Enhanced Absorption has similar cost and weight restrictions. The MQ4 [14] sensor costs $ 12, but has an accuracy range of ± 30,000 ppb, which makes it less suitable for inversion analysis. Current NDIR sensor technology was attractive due to its low-cost and weight, which make it suitable for mass deployment.

2.2 Remote Sensing with Low-Cost Multispectral Camera

While in-situ measurements are useful for making direct atmospheric observations, remote sensing is a powerful tool for characterizing a large surface area. Remote sensing [17, 18] operates on the basic principle that electromagnetic radiation (EM) from the sun is either transmitted, absorbed or reflected by a surface. A standard camera records the reflected light energy in the visible portion of the spectrum. However, the visible signature does not contain adequate information to characterize the photosynthetic activity, and thus carbon contribution of vegetation. Therefore, a larger portion of the EM spectrum, including the infrared region, was considered. All vegetation has photosynthetically active radiation (PAR), in the visible portion of the EM spectrum (400-700 nm) [19, 20]. However, beyond these wavelengths, a photon of light no longer contains enough energy to be used by plants in photosynthesis, as shown schematically in Figure 3a. Healthy green vegetation is expected to reflect large amounts of near infrared light (NIR), and low amounts of red, green and blue light. This ratio of NIR to visible reflectance is a measure of the photosynthetic activity of the vegetation [21]. The multispectral imaging system was designed and constructed with the goal of measuring this ratio.

The Raspberry Pi camera shown in Figure 3b is capable of recording reflected light energy in both the visible and near infrared regions of the EM spectrum (400-750 nm). This portion of the spectrum was divided into four bands of distinct wavelength ranges: near infrared, red, green and blue. Red, green and blue filters were used to block out all wavelengths except those of its respective colors. I used the well-known and cost-effective Nitecore 25.4 mm filters, that allowed the narrowest bands of light through to maximize the distinction and clarity in the analysis. The Neewer 58 mm high quality optical glass infrared lens filter was used to block all wavelengths beneath 720 nm. The various filters quantify the reflected energy in each of these four bands and obtain the spectral reflectance of the surface: the reflected energy as a function of wavelength.

The camera was connected to the serial interface port on the Raspberry Pi. The Raspberry Pi allows for storage through a microSD card, wireless Ethernet connection for network, and an HDMI and camera serial interface port. Raspbian software was written on the microSD

card using a win32 disk imager. Raspbian was chosen over other operating systems as it is the most user-friendly, and well adapted for the Raspberry Pi. Both still pictures and videos were taken using the commands in Raspbian. Table 2 compares the performance characteristics of the Raspberry Pi camera with commercially available multispectral systems [22, 23]. The Rasberry Pi camera and filters cost (\$ 80) and weigh 3 g, which makes them suitable for mass deployment.
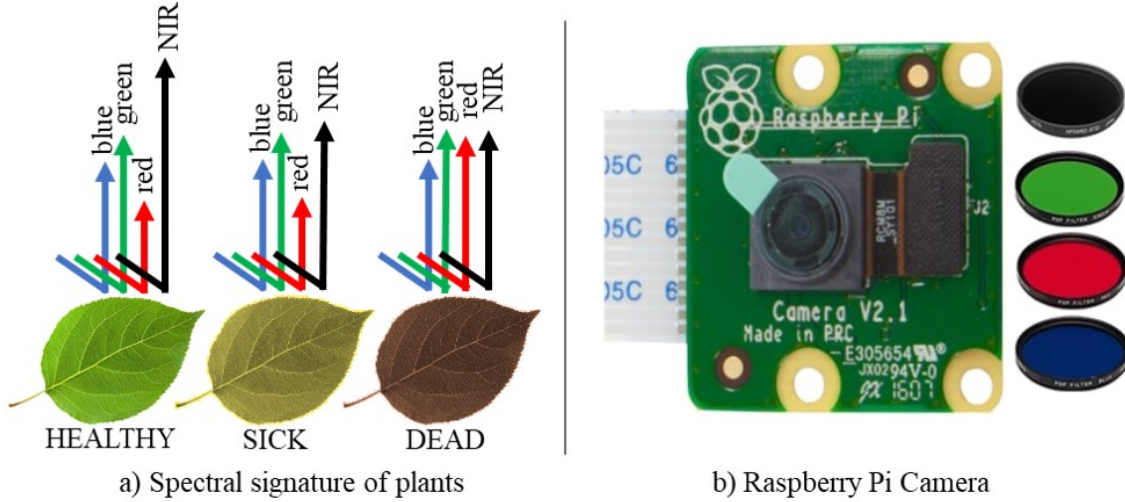

Figure 3: a) Spectral signature of healthy, sick and dead plants b) Raspberry Pi 3 Model B camera with the serial interface port connector, and the near IR, green, red, and blue filters (ordered from top to bottom)

2.3 Construction and Programming of Low Powered Drones

Commercially available CO_2 sensors [12, 15] cost over \$60,000 and weigh close to 25 kg. Due to the cost and weight of commercial sensors, measurements are limited to a few installations on platforms such as towers and ground-based vehicles. This severely restricts the use of these sensors to predict emission inventories using a top-down approach. While stationary towers provide stable, high accuracy, continuous measurements, the measurement height of towers is limited and generally small relative to the spread and range of a plume. Lack of mobility increases cost due to the need for a dense network of sensors. Ground based vehicles provide mobility, but the sensor data is affected by interactions with nearby buildings and ground level turbulence. Current measurement platforms clearly limit the ability of sensor to make accurate measurements representative of the entire boundary layer.

Low-powered unmanned aerial vehicles (UAV) or drones allow measurements that span the entire boundary layer without sacrificing control and reliability. Drone mobility and autonomy maximizes efficiency, as well as provides a stable platform for measurement. Their ability to survey areas that are otherwise difficult to access optimizes them for atmospheric measurements [19]. The development of low-cost and light-weight NDIR sensors allow for alternative measurement platforms such as drones.

A quadcopter was designed and constructed to allow for mounting of the low-cost sensor and to provide a stable platform for the multispectral imaging camera while in flight. Figure 4 is a photograph of the front and top view of the final quadcopter along with the sensors, just before a test flight. A carbon fiber frame was used for rigidity and strength, and the propellers were powered with 2300 KV brushless motors. Motors were installed such that non-adjacent motors rotate in opposite directions for controlled vertical movement of the quadcopter. Electronic speed controllers (ESCs) were attached to the four motors to ensure precise and smooth shifts in motor speed. A CC3D board was used as the flight controller due to its small volume, affordability, and vast popularity, and a 7.5V battery was placed above the drone and attached through the frame to a power distribution board.
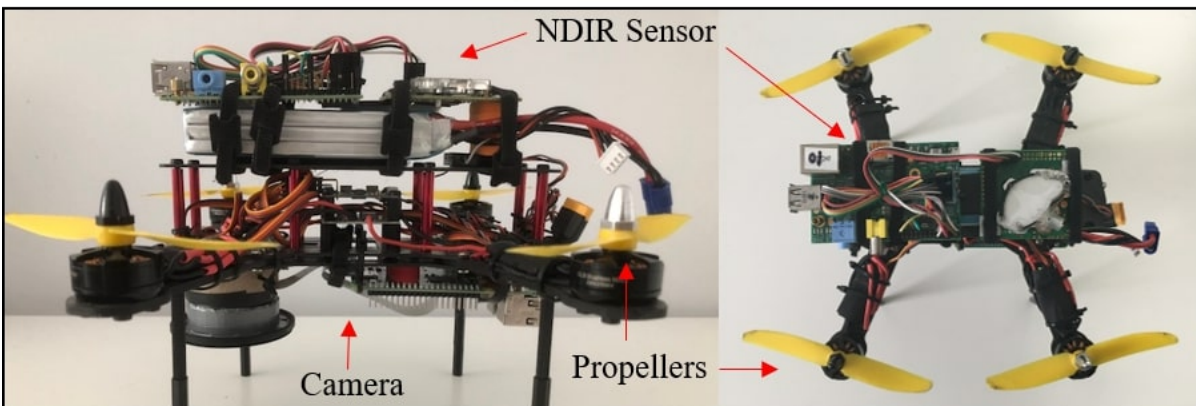

Figure 4: Side and top views of the quadcopter just before test flight. The NDIR sensor was mounted on top, while the imaging camera was attached underneath the drone.

The drone was designed with central attachment points to accommodate the low-cost sensors/camera. Propellers were adjusted to minimize the turbulence resulting from prop-wash. ESC's were incorporated and motor design was chosen in order to maximize stability and control of the drone while making measurements. The NDIR sensor was secured on top of

the drone, while the multispectral imaging system was mounted horizontally under the drone body using double sided tape to isolate electrical components and maintain stability. To avoid damaging the sensors, standoffs were mounted beneath each propeller to prevent contact while landing and taking off. The central placement of the sensors kept them unaffected by the prop-wash of the peripheral propellers.

Table 2: Comparison of performance characteristics of current low-cost camera with commercially available systems. Cost and weight analysis of various drone parts.

Remote Sensing Camera	Raspberry Pi Cam	Nano Hyper[22]	BaySpec [23]	Drone Part	Cost	Weight (g)
Pixel Size	1.4 μ m	2.2 nm	-	Motors/ESCs	$ 48	
# of bands	4	270	8	Power Board	$ 16	317
Wavelength nm	400-750	400-1000	400-1000	CC3D Board	$ 20	
Weight (g)	3	500	220	Battery	$ 16	174
Cost	$ 25	$ 50,000	$ 5,000	DXe Spectrum	$ 90	-

The total cost of the quadcopter, summarized in Table 2 was less than $ 200. The quadcopter weighs approximately 317 g and can accommodate another 300 g without losing stability and mobility. Since the sensors cost $ 200 and weigh less than 100 g, this system allows large-scale deployment of sensors on both mobile drone based platforms and stationary platforms for atmospheric CO_2 measurements and monitoring of vegetation.

2.4   Atmospheric Chemical Transport Model

In order to estimate emission inventories, concentration measurements have to be combined with atmospheric transport models in an inversion framework. Atmospheric models simulate the dispersion and transport of greenhouse gases from a source (transportation sector or power plant) to the sensor. In this research, Gaussian Plume Dispersion [24, 25] models were used to estimate the concentration of a gas at a location with coordinates (x,y,z) using a diffusion equation.

$$c(x, y, z) = \frac{q}{2\pi U \sigma_y \sigma_z} exp\left[-\frac{y^2}{2\sigma_y{}^2} \right] \left\{ exp\left[-\frac{(z-h)^2}{2\sigma_z{}^2} \right] + exp\left[-\frac{(z+h)^2}{2\sigma_z{}^2} \right] \right\} + c_{bg} \qquad (1)$$

where, c is the measured concentration, c_{bg} is the background concentration, x is the stream wise distance of the sensor from the source, y is the crosswind distance of the sensor from

the plume centerline, z is the height of the sensor above the ground, q is the strength of the source, U is the average wind speed in the stream wise direction, σ_y and σ_z are dispersion coefficients based on atmospheric stability, and h is the stack height. The plume model assumes steady state atmospheric conditions and emissions are constant and continuous in time. The plume dispersion equation (Eq. 1) can be alternatively written as

$$c = \left(c/q\right)_{est}q + c_{bg} \tag{2}$$

where, the ratio $(c/q)_{est}$ represents the influence of the source on the sensor (footprint).

Influence Functions

Figure 5 shows the role of wind speed and atmospheric stability on the computed influence functions $(c/q)_{est}$, plotted in units of $ppm/(\mu mol/m^2/s)$. The influence functions were computed for a point measurement located at the origin (0,0) with a height of 50 m. The wind was assumed to be from the East (right to left).
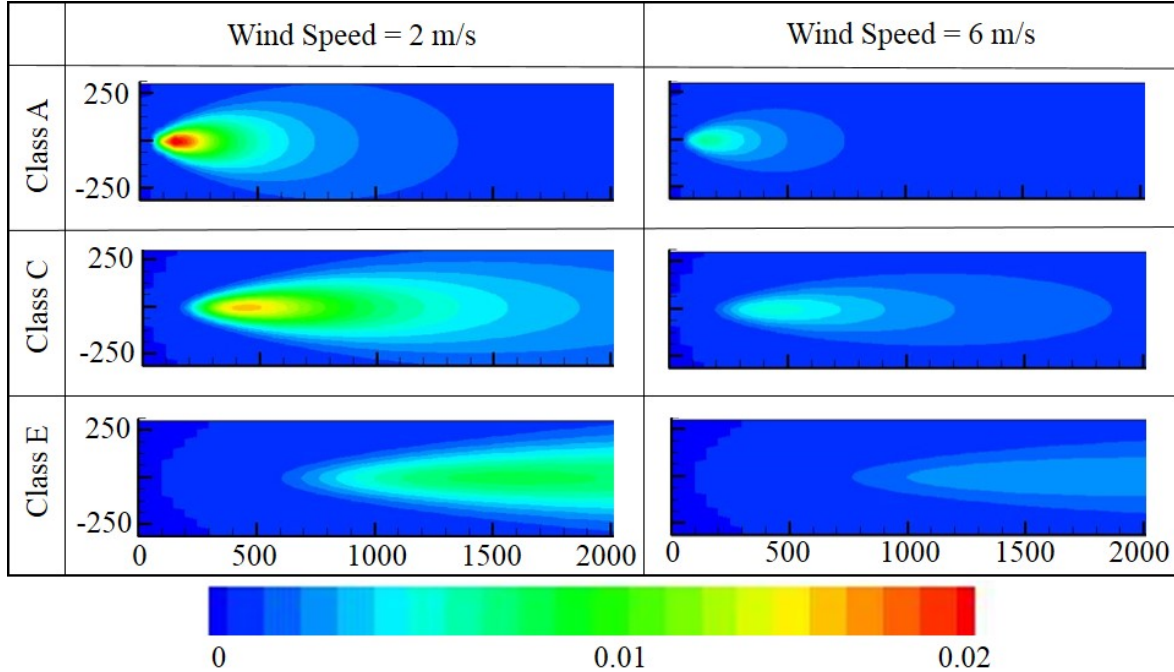

Figure 5: Influence Function $(c/q)_{est}$ in units of $ppm/(\mu\,mol/m^2/s)$ plotted for two wind speeds $(2,\,6\,m/s)$ and three atmospheric stability classes (unstable, neutral and stable).

The footprint strength reduces as the wind speed increases. The magnitude of the influence function was inversely proportional to wind speed (See Eq. 1). A source would have a

larger influence on the measurements as the wind speed reduces from 6 m/s to 2 m/s. For unstable stability class A, the footprints expand further in a direction perpendicular to the wind speed, as compared to neutral stability class C. Along the wind direction, the footprint patterns extend further as stability class increases from A to E.

Ill-posed Inverse Problem

For the case of multiple sources (m) and multiple sensors (n), Eq. 2 can be written as

$$\{c\}_{n\times1} = [H]_{n\times m}\{q\}_{m\times1} + \{c_{bg}\}_{n\times1} \tag{3}$$

$$\{y\}_{n\times1} = \{c\}_{n\times1} - \{c_{bg}\}_{n\times1} = [H]_{n\times m}\{q\}_{m\times1} \tag{4}$$

where, $\{c\}$ and $\{c_{bg}\}$ are downwind and background measurement vectors (size n) respectively obtained using the low-cost sensor, $\{q\}$ represents the unknown source strength vector (size m) and $[H]$ represents an $n \times m$ matrix of the estimated ratio terms ($(c/q)_{est}$), also referred to as the footprint matrix. Vector $\{y\}$ is the enhancement vector of size n. Eq. 4 represents a system of n equations with m unknowns. For an ideal system, the number of unknowns should be equal to the number of sensor measurements ($n = m$). Under such a scenario, Eq. 4 could be inverted to obtain the source strength vector. However, due to uncertainties in measurement data and transport model errors, the number of measurements should be much greater than the number of unknowns ($n >> m$). Under such scenarios, a least squares method [26] could be used to minimize the residual and to estimate the emissions. In practice, the number of measurements are rarely greater than the number of unknowns.

The size of the domain that covers Washington DC / Baltimore is approximately $130\,km\times 100\,km$. Dividing this domain with a square mesh of $1\,km^2$, gives rise to $13,000$ cells (number of unknowns) for which the flux has to be estimated (m). The number of hourly measurements (n) are usually of the order of 100. As a results, the number or unknowns is much greater than the number of sensor measurements ($m >> n$). This results in an ill-posed system of equations that does not have a unique solution. Additional information in the form or initial guess, regularization and likelihood / variability is needed to inform the emission inventories [27]. For such scenarios, a Bayesian Kalman Filter methodology [27] is proposed to constrain the fluxes starting with an initial guess (prior).

2.5 Bayesian Inversion Analysis and Uncertainty Quantification

Optimum posterior estimates of fluxes were obtained by minimizing the cost function J

$$J(\boldsymbol{q}) = \frac{1}{2}\Big[(\boldsymbol{q} - \boldsymbol{q_p})^T \boldsymbol{P}^{-1}(\boldsymbol{q} - \boldsymbol{q_p}) + (\boldsymbol{Hq} - \boldsymbol{y})^T \boldsymbol{R}^{-1}(\boldsymbol{Hq} - \boldsymbol{y})\Big] \tag{5}$$

where, $\boldsymbol{q_p}$ is the first guess of the emissions (prior) usually obtained from a bottom-up inventory; $\boldsymbol{P}$ is a matrix that represents the uncertainties in our prior knowledge; and $\boldsymbol{R}$ is a matrix that represents uncertainties in the dispersion model and observations. Our goal is to use observations to constrain / inform the emission inventory (assumed to be static in time). Minimization of Eq. 5 leads to the well-known Kalman filter equations [27, 28]

$$\boldsymbol{q} = \boldsymbol{q} + \boldsymbol{K}(\boldsymbol{y} - \boldsymbol{Hq}) \tag{6}$$

$$\boldsymbol{K} = \boldsymbol{PH}^T(\boldsymbol{HPH}^T + \boldsymbol{R})^{-1} \tag{7}$$

$$\boldsymbol{P} = (\boldsymbol{I} - \boldsymbol{KH})\boldsymbol{P} \tag{8}$$

Eq. 6-8 are the evolution equations of the Kalman filter. Here, $\boldsymbol{K}$ is the Kalman gain matrix that modulates the correction being applied to the emission $\boldsymbol{q}$ (Eq. 6) as well as the evolution of prior uncertainties(Eq. 8). The initial uncertainty in the emissions follows an exponential model

$$\boldsymbol{P}_{i,j} = \sigma_i \sigma_j e^{-d_{i,j}/L} \tag{9}$$

where, $d_{i,j}$ is the distance between pixels i and j, and L is the correlation length. The model data uncertainty matrix $\boldsymbol{R}$ was assumed to be diagonal with a standard deviation of the Gaussian errors set at $5\,ppm$.

3 Results and Discussion

In this section, I test and demonstrate the accuracy of our low-cost CO_2 sensors and present results from our multispectral camera to identify biogenic emissions. Collected data was combined with the transport model to estimate and attribute emissions in Washington DC.

3.1 Statistical Analysis

An NDIR sensor was collocated with an LGR sensor near a site at the University of Maryland and a linear regression analysis was conducted to determine the accuracy of the NDIR sensor. The Los Gatos Research (LGR) sensor is a well-known and widely used carbon dioxide sensor, capable of predicting concentrations with an accuracy of $\pm$ 2 ppb.

An unpaired two-tailed T-test was conducted (Figure 6) to compare measured CO_2 concentrations from the NDIR and LGR sensors. Before conducting this test, NDIR data was calibrated by adding the average of the difference between the two sensors to NDIR measurements. The similarity between the two sensors was statistically significant, with a p value of 0.99. However, the NDIR sensor does show a slightly higher degree of variance than the LGR. The mean difference in values between the two sensors was 1.4 ppm, barely significant considering the typical baseline of 390 ppm for atmospheric CO_2 measurements. The linear regression analysis (Figure 6) resulted in an R^2 of 0.94, indicating a high degree of correlation between the data streams from the two instruments. These results indicate the suitability of the NDIR sensor for inversion analysis
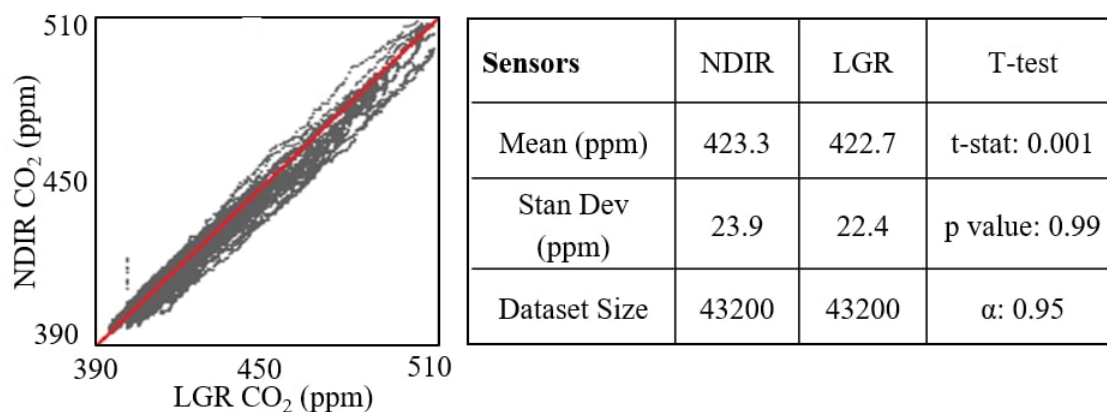

Sensors	NDIR	LGR	T-test
Mean (ppm)	423.3	422.7	t-stat: 0.001
Stan Dev (ppm)	23.9	22.4	p value: 0.99
Dataset Size	43200	43200	α: 0.95

Figure 6: Correlation of the low-cost NDIR data with LGR sensor data along with statistical analysis demonstrating sensor accuracy.

Seasonal Trends and Annual Variability

Figure 7 depicts three years of hourly averaged CO_2 data. The time in years is plotted on the x-axis and CO_2 concentration in ppm is plotted on the y-axis. A clear seasonal cycle is

visible in the data, similar to the seasonal trends seen in the Keeling curve (Figure 1). There is a consistent dip in CO_2 concentration during the summer months due to photosynthetic uptake. Concentrations return back to baseline values during winter months when photosynthetic activity ceases. The seasonal cycles observed in Figure 7 further validates the sensors ability to capture important fluctuations.
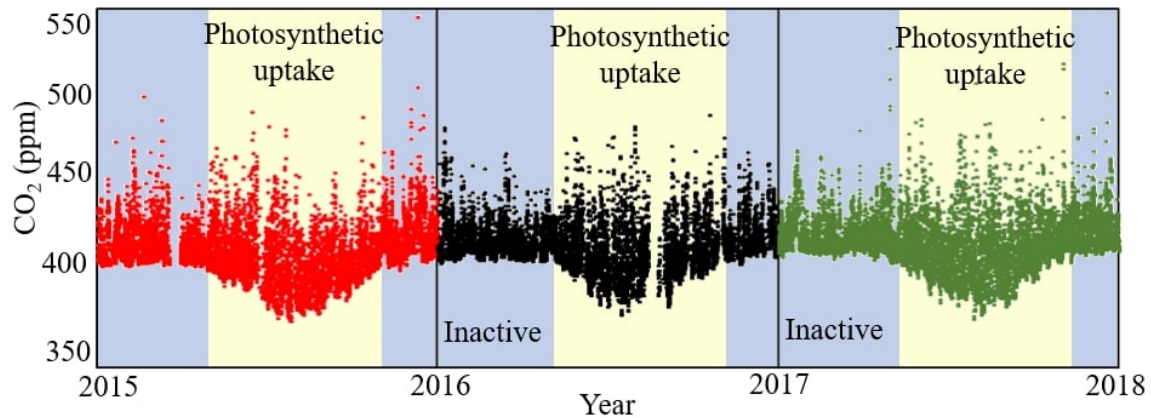

Figure 7: Hourly averaged CO_2 data plotted over a three year period showing the seasonal cycles including photosynthetic uptake during the summer season and higher concentrations during the inactive winter months.

Diurnal Cycle and Traffic Patterns

CO_2 data for February 2016 was averaged by hour and plotted to understand the daily variations in the measurements. Figure 8a reveals a distinct peak in carbon dioxide concentration at around 7 am, and a low at 4 pm (EST). This clearly demonstrates the presence of a diurnal cycle in the measurement data; during the day as the sun heats the earth's surface, the boundary layer expands resulting in the low average concentrations during afternoon hours (4pm EST). On the other hand, at night when the earth's surface cools down, the boundary layer is compressed resulting in peak gas concentrations in the morning.

Figure 8b is a plot of CO_2 data averaged by hour for a single weekday in February. A closer look at the CO_2 sensor data for the weekday shows small jumps in concentration between 7-9 am and again between 4-6 pm EST, superimposed on the diurnal trend (shown in Figure 8b between the dotted lines). These jumps coincide with the rush hour traffic in Washington DC and are attributed to the increased transportation activity. Figure 8c is a similar plot

for a single weekend in February. The CO_2 weekend data shows the corresponding jumps in the signal at 12 pm and 8 pm EST indicating differences in traffic patterns on weekdays and weekends. Diurnal trends and traffic patterns in sensor data demonstrate the sensitivity of the NDIR technology to capture daily fluctuations in CO_2 levels.
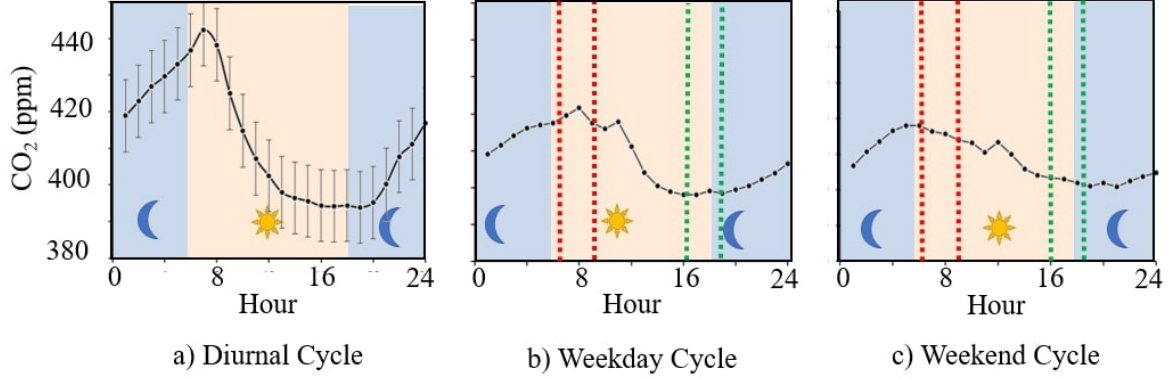

Figure 8: a) Observed CO_2 diurnal cycle. Spikes in CO_2 data for b) weekdays and c) weekends correlate with traffic patterns in Washington DC

3.2 Estimating the Biological Ecosystem

Quantifying the biological ecosystem (sources and sinks) is necessary to accurately estimate city-wide emissions. The carbon exchange of these systems is directly related to their photosynthetic and respiring activities. I present the multispectral camera imaging data to identify surfaces containing live vegetation. Live green plants absorb solar radiation in the photosynthetically active radiation (PAR) region of the spectrum (400 to 700 nm) to use as energy for photosynthesis. At wavelengths longer than 700 nm, a photon no longer contains enough energy to synthesize organic molecules. Therefore, live vegetation generally appears dark in the PAR, and bright in the near-IR. This concept to identify vegetation can be quantified using the normalized difference vegetation index (NDVI) , defined as

$$NDVI = (DN_{NIR} - DN_{RED})/(DN_{NIR} + DN_{RED}) \qquad (10)$$

where, DN_{NIR} is the digital number of reflectance in the near infrared band and DN_{RED} is the reflectance in the red band. NDVI can range from [-1,1]. Live green vegetation has high DN_{NIR}/DN_{RED} ratios, and its NDVI approaches 1. On the other hand, asphalt and soil would have an NDVI closer to zero, while dead grass and bodies of water would have an
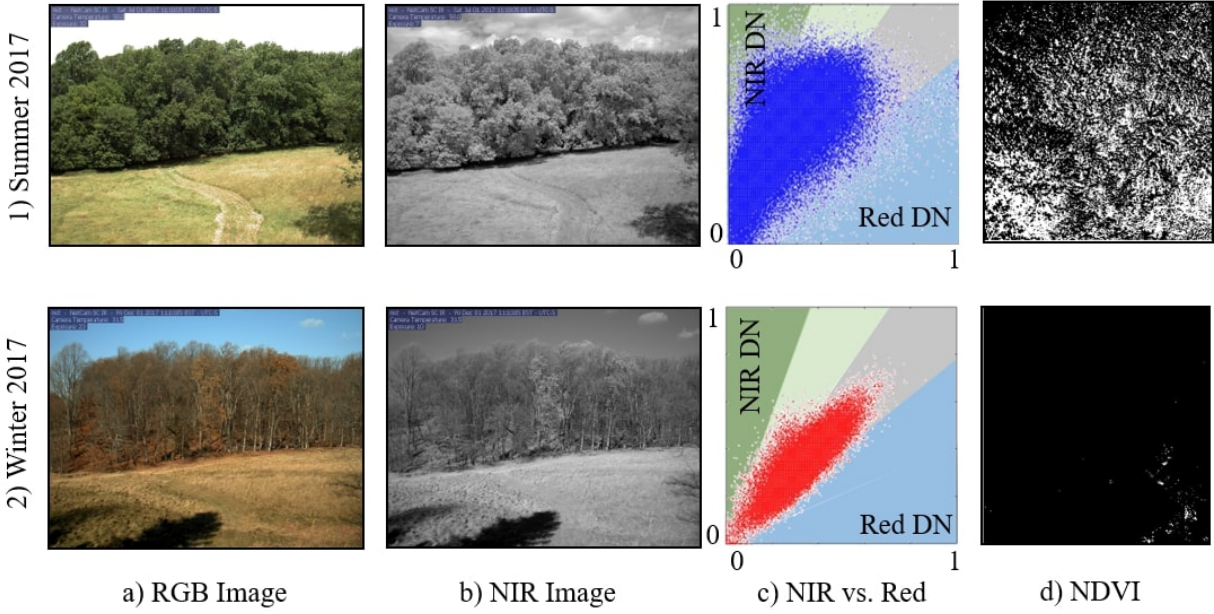
NDVI closer to -1.

Figure 9: Vegetation spectral data collected from a forest near Washington DC for Summer (top row) and Winter (bottom row), 2017. The first and second column show the raw RGB and IR images of various vegetation sites, the third column is a plot of red (x-axis) versus the near infrared reflectance (y-axis). The fourth column displays the normalized difference vegetation index for the site.

Figure 9 presents spectral data from a forest in Gaithursburg, Md for 2017 (Summer and Winter months). Figure 9a, b is the RGB and IR image for the vegetation from July 2017, when photosynthetic activity is expected to be large. Figure 9c plots the intensity of the NIR signal versus the intensity of the Red signal. Active vegetation contains cellulose, proteins and other minerals giving it high reflectance in the NIR and low reflectance in the red. Further, plant pigments such as chlorophyll and caretenoids absorb red light, but reflect NIR light as it lacks enough energy to be used in photosynthesis. Figure 9c indicates a high density in the dark green portion, where the ratio of NIR to Red reflectance is high. The corresponding NDVI (Figure 9d) is very bright, again corresponding to high photosynthetic activity. A similar analysis was conducted on RGB and IR images (Figure 9e, f) from Winter, 2017. Figure 9g indicates an NIR:Red ratio closer to 1, and dark NDVI indicating low photosynthetic levels.

3.3 Emission Inventory for Washington DC

Figure 10a shows a Google image of the domain around Washington DC and Baltimore. Drone flights and tower based CO_2 measurements were made at the location shown by red dots. The blue dots on the image show the location of the multispectral camera measurements. The measurement data from the low-cost sensors was combined with an atmospheric transport and dispersion model (plume model) and meteorological data as part of an inversion framework to estimate an emission inventory. The plume model was driven with archival meteorological data [29] for February 2017.

a) Google Earth image of domain & sensor locations

b) Composite footprints ($\frac{ppm}{\mu mol/m^2/s}$) for February, 2017
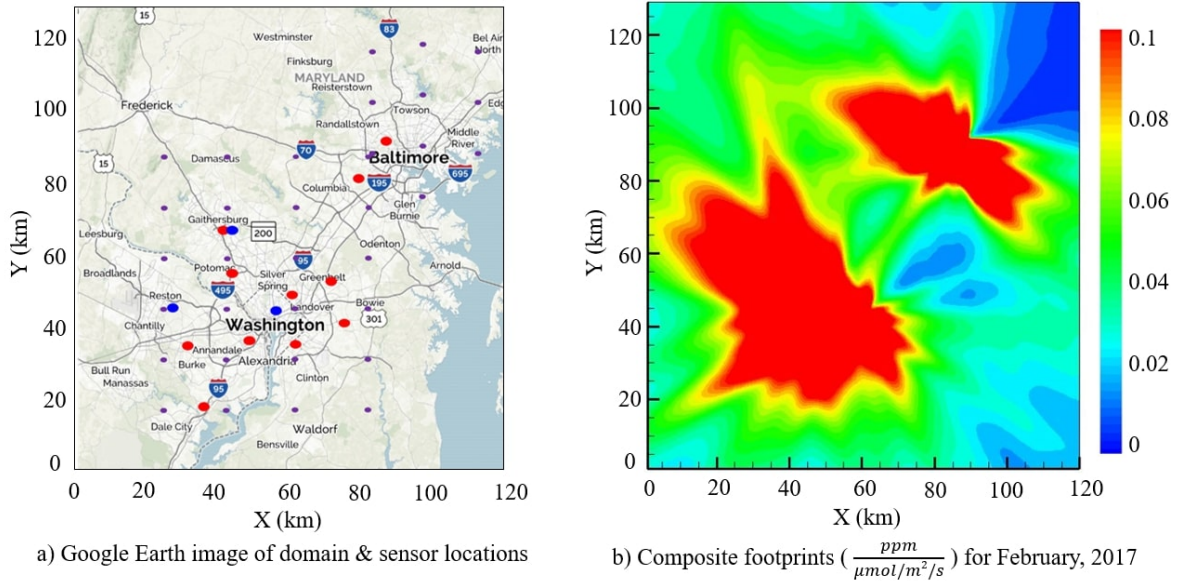
Figure 10: a) Google Earth image of the domain surrounding Washington DC & Baltimore used for estimating the emissions. The red symbols indicate the location of the point sensor measurements and blue dots mark the site at which spectral data was collected b) Integrated footprints ($ppm/(\mu mol/m^2/s)$) for an entire month for the drone and tower based measurements.

The integrated footprints ($ppm/(\mu mol/m^2/s)$) for the drone and tower based measurements are shown in Figure 10b. The footprint map shows good coverage over the entire domain and very high sensitivities $> 0.08\,ppm/(\mu mol/m^2/s)$ in the DC metropolitan region as well as Baltimore city. Lack of coverage in the south-east and north-east portions of the domain is due to lack of winds from that direction.

3.4   Uncertainty Analysis

Figure 11a shows the predicted emissions ($\mu\,mol/m^2/s$) from Washington DC obtained from the inversion methodology. Comparison of these results with the domain of interest shown in Figure 10a, clearly indicate that CO_2 emissions occur primarily from the transportation sector. Smaller emissions from the urban domain are also visible, while the red dots indicate large point sources such as power plants (north of Washington DC). Total CO_2 emissions over the entire domain were 101,000 $\mu\,mol/s$. These results are consistent with our earlier findings and demonstrate that the methodology proposed in this paper can be used to accurately predict emissions in a megacity and quantify individual sources.
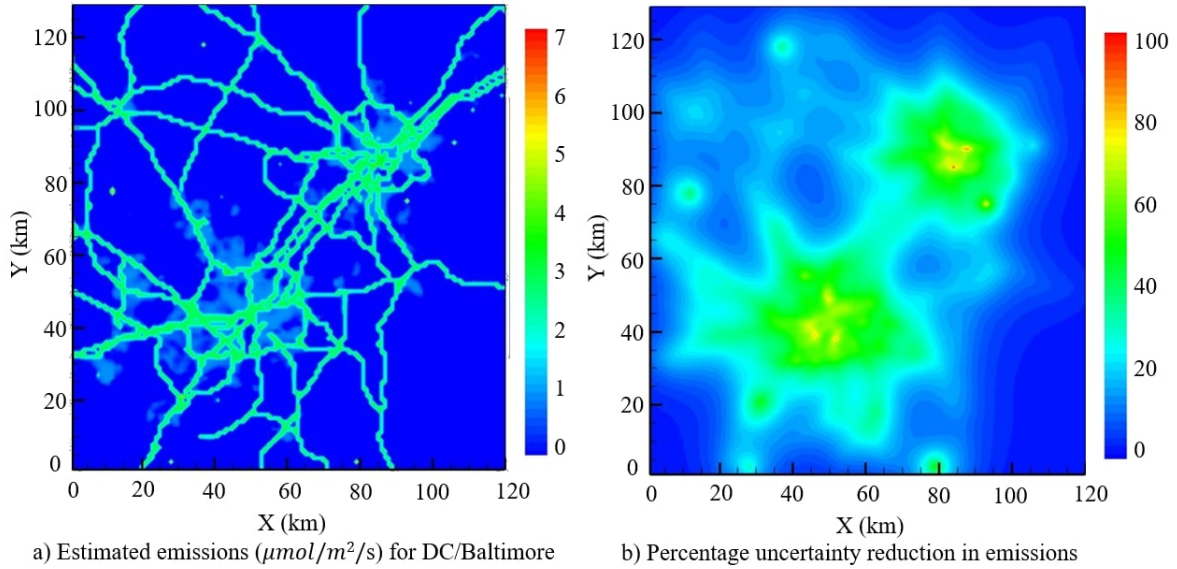

a) Estimated emissions ($\mu mol/m^2/s$) for DC/Baltimore   b) Percentage uncertainty reduction in emissions

Figure 11: a) Predicted CO_2 emissions inventory for Washington DC using the sensor data and mathematical models, indicating large emissions from the transportation sector, b) Uncertainty reduction through the use of atmospheric measurements predicted from Kalman Filter approach.

The initial uncertainty in the emissions was described earlier in Eq. 9. With each iteration of the Kalman Filter Eq. 6, the uncertainty in the emissions were advanced in time using Eq. 8. The uncertainty reduction was computed between the initial and final uncertainty matrices using the following equation.

$$\text{Uncertainty Reduction}(\%) = 100\Big[1 - \frac{\sqrt{diag(P_{initial})}}{\sqrt{diag(P_{final})}}\Big] \tag{11}$$

18

Figure 11b shows the uncertainty reduction plotted over the entire domain. Uncertainty reduction in the region close to the measurement locations were as high as 90 % due to the high sensitivity values of the footprint Figure 10b. The uncertainty reduction is significantly smaller outside the beltway. These results clearly demonstrate that the overall methodology can successfully estimate emissions and the related uncertainties.

4 Summary, Conclusions and Future Work

Half the world's population currently lives in cities, and another 2.5 million are expected to join them by 2050. With rapid urbanization leading to large population densities and high energy demands, cities are responsible for 70% of worldwide greenhouse gas emissions. The Paris agreement sets rigorous goals to limit global warming to less than 1.5 ^{0}C above pre-industrial levels. Anthropogenic CO_2 emissions must decline by 45% from 2010 levels by 2030, reaching net zero by 2050. But enforcement of these mitigation strategies requires specificity of targets and continuous monitoring of CO_2 emissions. In the worldwide effort to combat climate change, the ability to measure greenhouse gas emissions from large cities is a compulsory first step.

Commercially available sensor technology is either too expensive for mass deployment in cities, or lacks the accuracy to quantify overall emissions and pinpoint specific sources for further action. Current approaches based on numerical weather prediction to quantify emissions are computationally inefficient and memory intensive. Moreover, methods to distinguish between anthropogenic and biogenic emission do not exist. This report was motivated by the lack of low-cost sensors, well distributed and efficient platforms for mounting sensors, and appropriate mathematical models to estimate emissions from megacities.

Data from our low-cost sensors captured concentrations accurately a statistically significant 99% of the time. CO_2 data also distinctly illustrated a diurnal cycle, peaking during early morning hours and hitting lows during the afternoon, as well as identified weekday and weekend traffic patterns. Comparison of data from our low-cost sensor with state-of-the-art equipment revealed a linear relationship with a correlation coefficient of 0.94. The multispectral imaging system successfully distinguished between vegetation of varying photosynthetic

activity and thus identified their relative roles in the carbon cycle. Drone construction, calibration and programming culminated in successful and stable flight. The plume dispersion model and inversion tools were able to predict emission inventories for Washington DC, and highlighted a large CO_2 contribution from the transportation sector. Total CO_2 emissions over the entire domain were 101,000 $\mu\,mol/s$. Uncertainty reduction were as high as 90 %, indicating the success of the overall methodology.

Rockstrom et al. [30] outlines a rigorous carbon law to halve emissions every decade in order to remain well below the 2 ^{0}C warming limit. The IPCC [31] calls for gross emissions to decline from $\approx$ 40 $GtCO_2$/year by 2020, to $\approx$ 24 $GtCO_2$/year by 2030, $\approx$ 14 $GtCO_2$/year by 2040,and $\approx$ 5 $GtCO_2$/year by 2050. The risks of failing to achieve these goals cover a range of climate-related risks to health, livelihood, biodiversity, sea levels and weather events. By developing the sensor-mounted drone and atmospheric plume model, I have started an effort to reduce urban emissions through the continuous monitoring of carbon dioxide concentrations. I construct the tools for and demonstrate the efficiency and success of a comprehensive measurement system to enforce government-set carbon laws and mitigation strategies, taking the first step toward combating climate change.

In the future, I aim to continue deploying low-cost sensor networks in other metropolitan cities and estimate their emission inventories. The emission patterns for cities with complex meteorological patterns, manufacturing and production based economies, varying transportation patterns and different urban-suburban distributions will be studied.

5   Acknowledgments

References

[1] National Research Council. (2010). *Verifying greenhouse gas emissions: methods to support international climate agreements*. National Academies Press.

[2] Staudt, A., Huddleston, N., & Kraucunas, I. (2008). Understanding and Responding to Climate Change: Highlights of National Academies Reports.

[3] Pachauri, R. K., Allen, M. R., Barros, V. R., Broome, J., Cramer, W., Christ, R., ... & Dubash, N. K. (2014). *Climate change 2014: synthesis report. Contribution of Working Groups I, II and III to the fifth assessment report of the Intergovernmental Panel on Climate Change* (p. 151). IPCC.

[4] Ramaswamy, V., Schwarzkopf, M. D., Randel, W. J., Santer, B. D., Soden, B. J., & Stenchikov, G. L. (2006). Anthropogenic and natural influences in the evolution of lower stratospheric cooling. *Science, 311*(5764), 1138-1141.

[5] Field, C. B., Barros, V., Stocker, T. F., & Dahe, Q. (Eds.). (2012). *Managing the risks of extreme events and disasters to advance climate change adaptation: special report of the intergovernmental panel on climate change*. Cambridge University Press.

[6] Ramanathan, V. (1988). The greenhouse theory of climate change: a test by an inadvertent global experiment. *Science, 240*(4850), 293-299.

[7] Melillo, J. M. (2014). *Climate change impacts in the United States, highlights: US national climate assessment*. Government Printing Office.

[8] Tollefson, J. (2012). Megacities move to track emissions. *Nature, 492*(7427), 20.

[9] Nisbet, E., & Weiss, R. (2010). Top-down versus bottom-up. *Science, 328*(5983), 1241-1243.

[10] Gurney, K. R., Mendoza, D. L., Zhou, Y., Fischer, M. L., Miller, C. C., Geethakumar, S., & De la Rue du Can, S. (2009). High resolution fossil fuel combustion CO_2 emission fluxes for the United States. *Environmental science & technology, 43*(14), 5535-5541.

[11] Dr. Pieter Tans, NOAA/ESRL (www.esrl.noaa.gov/gmd/ccgg/trends/) and Dr. Ralph Keeling, Scripps Institution of Oceanography (scrippsco2.ucsd.edu/).

[12] Picarro User's Guide. (2011). *G2401 Analyzer for $CO_2/CO/CH_4/H_2O$.*

[13] LI-COR. (2015). *LI-7700 Open Path CH_4 Analyzer.*

[14] Analog Gas Sensor (MQ4)," Robot Wiki, (2015).

[15] Los Gatos Research. (2015). *Ultraportable Greenhouse Gas Analyzer (CH4, CO_2, H_2O).*

[16] Shuman, F. G. (1978). Numerical weather prediction. *Bulletin of the American Meteorological Society, 59*(1), 5-17.

[17] Khan, A., Schaefer, D., Tao, L., Miller, D. J., Sun, K., Zondlo, M. A., ... & Lary, D. J. (2012). Low power greenhouse gas sensors for unmanned aerial vehicles. *Remote Sensing, 4*(5), 1355-1368.

[18] Roldán, J. J., Joossen, G., Sanz, D., del Cerro, J., & Barrientos, A. (2015). Mini-UAV based sensory system for measuring environmental variables in greenhouses. *Sensors, 15*(2), 3334-3350.

[19] Gates, D. M., Keegan, H. J., Schleter, J. C., & Weidner, V. R. (1965). Spectral properties of plants. *Applied optics, 4*(1), 11-20.

[20] Clark, J. B., & Lister, G. R. (1975). Photosynthetic action spectra of trees: II. The relationship of cuticle structure to the visible and ultraviolet spectral properties of needles from four coniferous species. *Plant Physiology, 55*(2), 407-413.

[21] Sonnentag, O., Hufkens, K., Teshera-Sterne, C., Young, A. M., Friedl, M., Braswell, B. H., ... & Richardson, A. D. (2012). Digital repeat photography for phenological research in forest ecosystems. *Agricultural and Forest Meteorology, 152*, 159-177.

[22] Nano-Hyperspec. (2016). *Small light airborne hyperspectral sensor DataSheet.*

[23] BaySpec. (2014). *Snapshot hyperspectral imager DataSheet.*

[24] Ermak, D. L. (1977). An analytical model for air pollutant transport and deposition from a point source. *Atmospheric Environment, 11*(3), 231-237.

[25] Griffiths, R. F. (1994). Errors in the use of the Briggs parameterization for atmospheric dispersion coefficients. *Atmospheric Environment, 28*(17), 2861-2865.

[26] Lawson, C. L., & Hanson, R. J. (1995). *Solving least squares problems* (Vol. 15). Siam.

[27] Jacob, D. J. (2007). Lectures on inverse modeling. *Harvard University.*

[28] Lermusiaux, P. F. (2006). Uncertainty estimation and prediction for interdisciplinary ocean dynamics. *Journal of Computational Physics, 217*(1), 176-199.

[29] Smith, A., Lott, N., & Vose, R. (2011). The integrated surface database: Recent developments and partnerships. *Bulletin of the American Meteorological Society, 92*(6), 704-708.

[30] Rockström, J., Gaffney, O., Rogelj, J., Meinshausen, M., Nakicenovic, N., & Schellnhuber, H. J. (2017). A roadmap for rapid decarbonization. *Science, 355*(6331), 1269-1271.

[31] Mechler, R., James, R., Wewerinke-Singh, M., & Huq, S. (2018). Loss and Damage in IPCC's report on Global Warming of 1.5 C (SR15). A summary.